Plasma Chemistry and Plasma Processing, Vol. 11, No. 1, 1991

Optical Emission Spectroscopy of Electron-Cyclotron-Resonance-Heated Helium Mirror Plasmas

K. L. Junck,[1] M. L. Brake,[1] and W. D. Getty[2]

Received October 2, 1989; accepted February 16, 1990

In this experiment emission spectroscopy in the 3000–5000 Å range has been utilized to determine the electron temperature (15–60 eV) and ion density ($2–5 \times 10^{11}$ cm^{-3}) of helium plasmas produced by the Michigan mirror machine[11] (MIMI). The plasma is generated and heated by whistler-mode electron-cyclotron resonance (ECR) waves at 7.43 GHz with 400–900 W power in 80-ms-long pulses. Gas fueling is provided at the midplane region by a leak valve with a range in pressure of 3×10^{-5} to 2×10^{-4} Torr. Emission line intensities are interpreted using a model of the important collisional and radiative processes occurring in the plasma. The model examines secondary processes such as radiation trapping, excitation transfer between levels of the same principle quantum number, and excitation from metastable states for plasmas in the parameter range of MIMI ($n_e = 1–6 \times 10^{11}$ cm^{-3}). From the analysis of line intensity ratios for neutral helium, the electron temperature is measured and its dependence upon the gas pressure and microwave power is determined. These temperatures agree with those obtained by Langmuir probe measurements. An analysis of the line intensity ratio between singly ionized helium and neutral helium yields a measurement of the ion density which is in good agreement with electron density measurements made by a microwave interferometer.

KEY WORDS: Emission spectroscopy; helium; ECR mirror plasma.

1. INTRODUCTION

ECR plasmas have become important sources for various areas of microelectronics processing such as chemical vapor deposition (CVD),[2] plasma stream etching,[3] ion implantation,[4] and reactive ion etching.[5] Recent works[6–8] have looked at the effect of weak magnetic mirror configurations on the plasma source and their usefulness in etching. ECR plasmas are also widely used as ion sources. In this paper we will characterize

[1] Department of Nuclear Engineering, Plasma Experimental Bay, University of Michigan, Ann Arbor, Michigan.

[2] Department of Electrical Engineering and Computer Science, Plasma Experimental Bay, University of Michigan, Ann Arbor, Michigan.

0272-4324/91/0300-0015$06.50/0

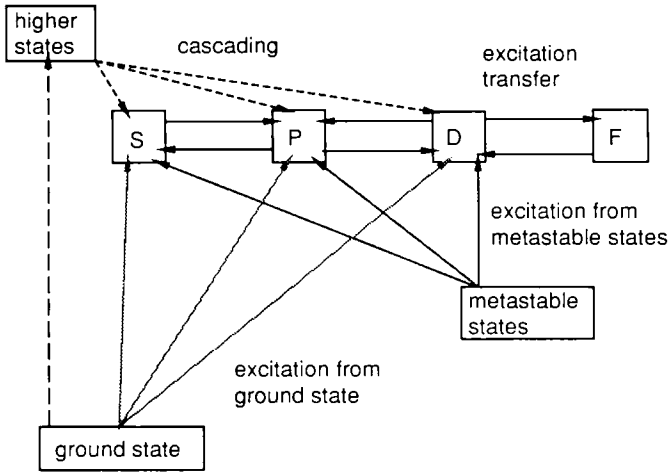

Fig. 1a. Schematic of processes that populate the levels in a group with the same principle and spin quantum numbers.

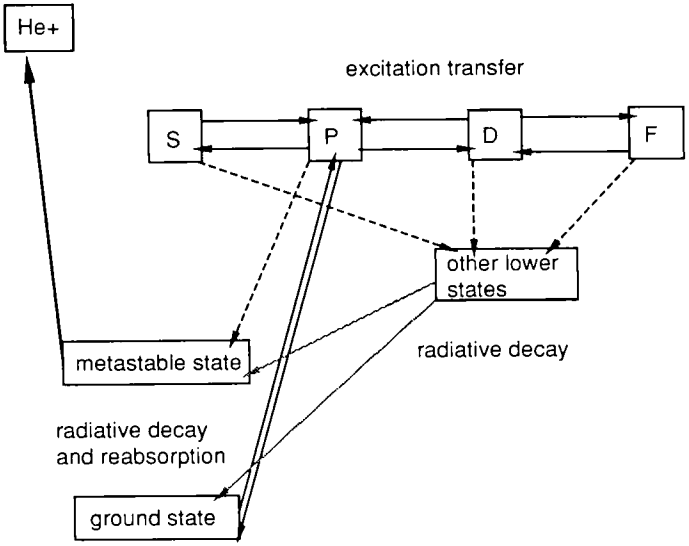

Fig. 1b. Schematic of processes that depopulate levels in a group.

the plasma of an ECR-heated magnetic mirror by optical emission spectroscopy. Current work has concentrated upon helium, but as more accurate cross-section data become available, this model will be extended to other gases such as Ar and O_2.

A method for measuring electron temperature using the relative intensities of neutral helium lines was first proposed by Cunningham[9] and further developed by Sovie[10] and Eastlund *et al.*[11] This method is based on the fact that the dependence of electron impact excitation on the electron energy is different between singlet and triplet lines of neutral helium. However, it was also determined that other secondary processes in a plasma may influence the helium line intensities significantly.[12-15] Theoretical modeling of helium plasmas performed by Brenning[16,17] and Drawin[18] will be extended to meet the needs of this experiment. In this analysis we will consider the effects of three secondary processes: (i) imprisonment of resonance radiation; (ii) excitation from metastable states; and (iii) excitation transfer collisions. A schematic of all the processes under consideration is shown in Fig. 1.

2. THEORY

2.1. Imprisonment Effects

Because of the large number of atoms in the ground state, the radiation emitted in a transition from a P state to the ground state may be absorbed and re-emitted by other ground-state atoms many times before escaping the plasma. This "imprisonment" results in an apparent increase in the probability that an excited atom will decay to a lower "nonresonant" state as well as an increase in the lifetime of the excited state.

The overall imprisonment can be represented by an "average degree of imprisonment" denoted I, which gives the total reduction in escaping resonance radiation. Phelps[19] has examined the theory of imprisonment in some detail for helium plasmas in cylindrical and slab geometries. Figure 4 of Phelps (Ref. 19) gives the escape factor g which is related to imprisonment by $I = 1 - g$. Note that for an optically thin plasma all radiation escapes and the degree of imprisonment is $I = 0$, while for an optically thick plasma no radiation escapes and the degree of imprisonment is $I = 1$.

The branching ratios for the $n^1P \rightarrow 1^1S$ transitions (see Fig. 2) can then be corrected for imprisonment. If an apparent branching ratio B^* is defined as the fraction of excitations to the n^1P levels that result in radiation which escapes, then

$$B^*_{n^1P \rightarrow 1^1S} = B_{n^1P \rightarrow 1^1S} \times [1 - I] \tag{1}$$

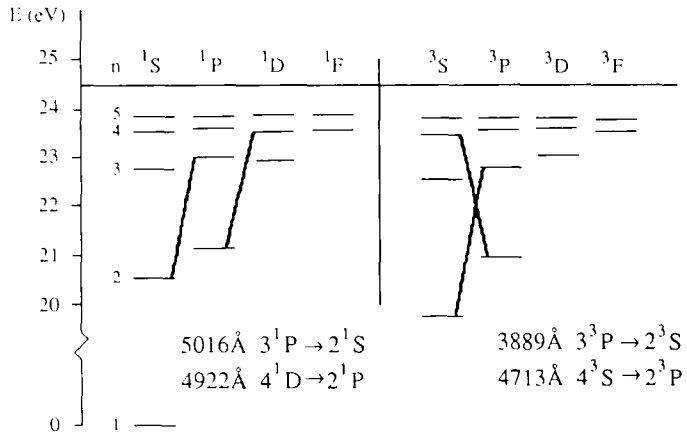

Fig. 2. Neutral helium energy level diagram. Transitions shown are those that will be used for the temperature determination.

where the branching ratio $B_{m\to n}$ (the fraction of decays from the upper level m that go to a certain lower level n) is given by

$$B_{m\to n} = \frac{A_{m\to n}}{\sum_{p<m} A_{m\to p}} \tag{2}$$

($A_{m\to n}$ is the Einstein coefficient of spontaneous decay from level m to level n). For low-lying P states ($n = 3, 4$) radiative decay is primarily to the 1^1S and 2^1S states, so

$$B_{n^1P\to 1^1S} + B_{n^1P\to 2^1S} = 1 \tag{3a}$$

and

$$B^*_{n^1P\to 1^1S} + B^*_{n^1P\to 2^1S} = 1 \tag{3b}$$

So, combining Eq. (1), (3a), and (3b) yields

$$B^*_{n^1P\to 2^1S} = B_{n^1P\to 2^1S} + (1 - B_{n^1P\to 2^1S}) \times I \tag{4}$$

Similarly, an apparent lifetime for the n^1P states can be written as

$$\tau^*_{n^1P} = \tau\left\{1 + I \times \left[\frac{A_{n^1P\to 1^1S}}{\sum_{k<1^1S} A_{n^1P\to k}}\right]\right\} \tag{5}$$

where $\tau(=1/A)$ is the radiative lifetime of the state. The choice of transition probabilities (Einstein coefficients) is discussed in the Appendix.

2.2. Metastable Excitation

An electron in the 2^1S or 2^3S state cannot move to a lower state without violating quantum mechanical selection rules. This results in these states having much longer radiative lifetimes (on the order of milliseconds) compared to higher states in which radiative decay is allowed (lifetimes on the order of nanoseconds). On the time scales we are considering, the metastable states may build up a non-negligible population. Thus, in this model, excitation occurs not only from the ground state but from the metastable states 2^1S and 2^3S as well. The total excitation rate constant to a level m can then be written as

$$K_m^* = K_{1^1S\to m} + \left[\frac{n_{2^1S}}{n_g}\right] K_{2^1S\to m} + \left[\frac{n_{2^3S}}{n_g}\right] K_{2^3S\to m} \tag{6}$$

where K_m^* is the "effective" excitation rate for level m; n_g, n_{2^1S}, n_{2^3S} are the densities of helium atoms in the ground (1^1S), singlet metastable, and triplet metastable states, respectively, and $K_{L\to m}$ is the excitation rate from a lower level L to an upper level m given by

$$K_{L\to m} = \frac{1}{n}\int f(\mathbf{v})\sigma_{L\to m}\mathbf{v}\, d^3v \tag{7}$$

The choice of $\sigma_{L\to m}$ for helium transitions is discussed in the Appendix and $f(\mathbf{v})$ is taken to be a Maxwellian distribution for electrons with n being the electron density.

To determine the ratios of the density of metastable atoms to the density of ground-state atoms (n_{2^1S}/n_g and n_{2^3S}/n_g) in Eq. (6), we construct the following rate equations. For the 2^1S metastable state, gain terms represent electron impact excitation of atoms in the ground state and 2^3S metastable state to an excited state followed by radiative decay to the 2^1S state, and loss terms are the result of electron impact excitation taking an atom out of the 2^1S state or ionization of an atom in the 2^1S state:

$$\frac{dn_{2^1S}}{dt} = \sum_d n_e n_g K_{1^1S\to d} B_{d\to 2^1S} + \sum_j n_e n_{2^3S} K_{2^3S\to j} B_{j\to 2^1S} - \sum_f n_e n_{2^1S} K_{2^1S\to f} - n_e n_{2^1S} K_{2^1S\to \mathrm{He}^+} \tag{8}$$

Similarly for the 2^3S metastable state:

$$\frac{dn_{2^3S}}{dt} = \sum_c n_e n_g K_{1^1S\to c} B_{c\to 2^3S} + \sum_i n_e n_{2^1S} K_{2^1S\to i} B_{i\to 2^3S} - \sum_h n_e n_{2^3S} K_{2^3S\to h} - n_e n_{2^3S} K_{2^3S\to \mathrm{He}^+} \tag{9}$$

The density ratio n_{2^1S}/n_g can be found by assuming steady-state conditions and combining Eq. (8) and (9):

$$\frac{n_{2^1S}}{n_g} = \frac{1}{\Delta}\left[\left(\sum_d K_{1^1S\to d} B_{d\to 2^1S}\right)\times\left(\sum_h K_{2^3S\to h} + K_{2^3S\to \mathrm{He}^+}\right) + \left(\sum_c K_{1^1S\to c} B_{c\to 2^3S}\right)\times\left(\sum_j K_{2^3S\to j} B_{j\to 2^1S}\right)\right] \tag{10}$$

$$\frac{n_{2^3S}}{n_g} = \frac{1}{\Delta}\left[\left(\sum_c K_{1^1S\to c} B_{c\to 2^3S}\right)\times\left(\sum_f K_{2^1S\to f} + K_{2^1S\to \mathrm{He}^+}\right) + \left(\sum_d K_{1^1S\to d} B_{d\to 2^1S}\right)\times\left(\sum_i K_{2^1S\to i} B_{i\to 2^3S}\right)\right] \tag{11}$$

where

$$\Delta = \left(\sum_h K_{2^3S\to h} + K_{2^3S\to \mathrm{He}^+}\right)\times\left(\sum_f K_{2^1S\to f} + K_{2^1S\to \mathrm{He}^+}\right) - \left(\sum_j K_{2^3S\to j} B_{j\to 2^1S}\right)\times\left(\sum_i K_{2^1S\to i} B_{i\to 2^3S}\right) \tag{12}$$

The results of Eqs. (10) and (11) are then used in Eq. 6 to determine the total excitation from the ground and metastable states.

2.3. Excitation Transfer

Excitation-transfer collisions between free electrons and He atoms in the upper line levels can occur during the natural lifetimes of the levels. Optically allowed transitions between levels of the same quantum number n have the largest cross sections. To determine the density of an upper level S state, we set up a rate equation where the loss terms are radiative decay from the S state and excitation transfer from the S state to the P state. Gain terms include excitation transfer from the P state as well as excitation from the ground and metastable states and cascading from higher states. Other processes, such as ionization from excited states, are negligible. Since highly excited states are essentially hydrogenic, we can use the calculations of Kingston[20] to determine this ionization rate, K_u [Eq. (7)] and for the parameter range under discussion the losses from radiative decay are much larger than ionization from n_S, i.e., $n_S/\tau_S \gg n_S n_e K_u$.

Thus the steady-state rate equation for the S state would be

$$\frac{-n_S}{\tau_S} - n_e n_S K_{S\to P} + n_e n_P K_{P\to S} + n_e n_g K_{1^1S\to S} + n_e n_{2^1S} K_{2^1S\to S} + n_e n_{2^3S} K_{2^3S\to S} + \sum_m n_e n_g K_{1^1S\to m} B_{m\to S} = 0 \tag{13}$$

where $\tau_S = 1/A_S$. Similar equations are written for the P, D, and F states. We can write these rate equations in a convenient matrix form. For the level $n = 4$ (singlet or triplet), we have

$$\begin{pmatrix} A & B & 0 & 0 \\ C & D & E & 0 \\ 0 & F & G & H \\ 0 & 0 & J & L \end{pmatrix} \begin{pmatrix} n_S \\ n_P \\ n_D \\ n_F \end{pmatrix} = n_g \begin{pmatrix} \alpha \\ \beta \\ \gamma \\ \delta \end{pmatrix} \tag{14}$$

where

$$A = -1/(n_e\tau_S) - K_{S\to P} \qquad B = K_{P\to S} \qquad C = K_{S\to P}$$

$$D = -1/(n_e\tau_P) - K_{P\to D} - K_{P\to S} \qquad E = K_{D\to P} \qquad F = K_{P\to D}$$

$$G = -1/(n_e\tau_D) - K_{D\to P} - K_{D\to F} \qquad H = K_{F\to D} \qquad J = K_{D\to F}$$

$$L = -1/(n_e\tau_F) - K_{F\to D}$$

$$\alpha = K^*_{1^1S\to S} + \sum K_{1^1S\to m} B_{m\to S} \qquad \beta = K^*_{1^1S\to P} + \sum K_{1^1S\to m} B_{m\to P}$$

$$\gamma = K^*_{1^1S\to D} + \sum K_{1^1S\to m} B_{m\to D} \qquad \delta = K^*_{1^1S\to F} + \sum K_{1^1S\to m} B_{m\to F}$$

with K^* given by Eq. (6) and K given by Eq. (7); $\tau(=1/A)$ is the radiative lifetime of the state and $K_{S\to P}$ and $K_{P\to D}$ are the rate coefficients for excitation transfer. The cross sections for these transitions are given by Drawin[21] using the Born-Bethe approximation:

$$\sigma_{mn} = 4\pi \frac{E_1^H}{E_{mn}} |z_{mn}|^2 \left(\frac{E_{mn}}{E_e}\right)^2 \left(\frac{E_e}{E_{mn}} - 1\right) \ln\left[1.5 \frac{E_e}{E_{mn}}\right] \tag{15}$$

where E_1^H is 13.59 eV (the ionization potential of hydrogen), E_e is the electron energy, E_{mn} is the energy difference between the levels m and n, and z_{mn} is the dipole length for the transition $m \to n$. The dipole lengths[22] used are for transitions in hydrogen and are assumed to be adequate for describing upper levels of helium. For the reverse processes, the rate coefficients are obtained using the principle of detailed balance. For example, $K_{P\to S} = (g_S/g_P)K_{S\to P} = (1/3)K_{S\to P}$, where g_S is the statistical weight of level S.

Solving Eq. (14) can be done by standard matrix techniques (e.g., Gauss-Jordan elimination[23]) and yields the density of a state in which all secondary processes have been taken into account. Equation (14) was solved for the $n = 3$ and $n = 4$ singlet and triplet states for various values of electron density and degree of imprisonment. The results of these calculations were used to predict the ratio of light emitted from a typical triplet state (3889 Å, for example) to a singlet state (5016 Å). This ratio is given in Figs. 3 and 4 as a function of electron temperature for several electron densities and values of imprisonment.

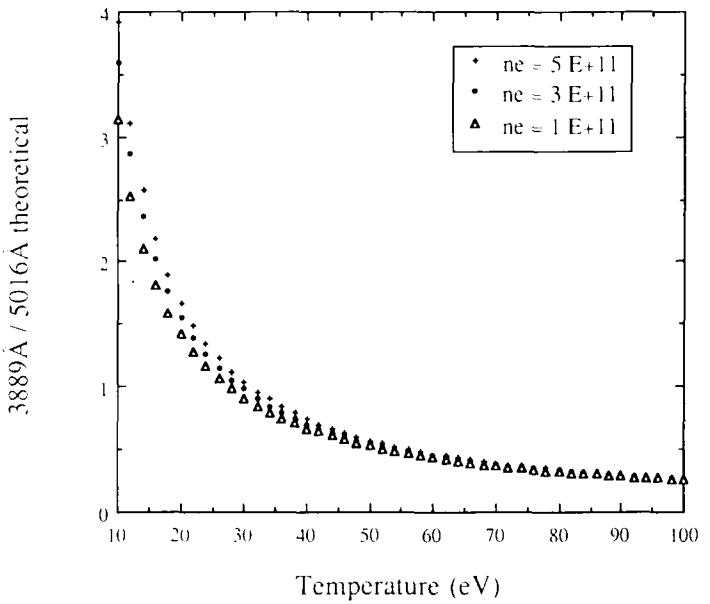

Fig. 3. Theoretical ratio of the 3889 Å ($3^3P \rightarrow 2^3S$) line intensity to the 5016 Å ($3^1P \rightarrow 2^1S$) line intensity versus electron temperature for several values of electron density, n_e (in units of cm^{-3}).

The model described above is used to determine the electron temperature by comparing the measured line intensity ratios with calculated ratios such as those shown in Figs. 3 and 4. The degree of imprisonment is determined from the optical depths of the resonance lines which are calculated from the measured neutral helium densities. The neutral helium density is measured with an ionization gauge. The electron density is measured by a 35-GHz microwave interferometer. Using the measured electron density and line intensity ratios, the electron temperature can be determined by a comparison with the calculated intensity ratios.

2.4. Helium II

One line from the spectrum of singly ionized helium is utilized to determine the ion density. The $n=4$ to $n=3$ transition of He II has a wavelength of 4686 Å. If the upper state of the He II line is populated only by excitation from the ground state of He II, and by simultaneous excitation and ionization of neutral helium, then the intensity of the line is given by

$$I_{4686} = \frac{n_4}{t_{\text{rad}}} B_{4\rightarrow 3} = B_{4\rightarrow 3} n_e n_g \left[K_{g\rightarrow 4} + \frac{n_+}{n_g} K_{+\rightarrow 4} \right] \tag{16}$$

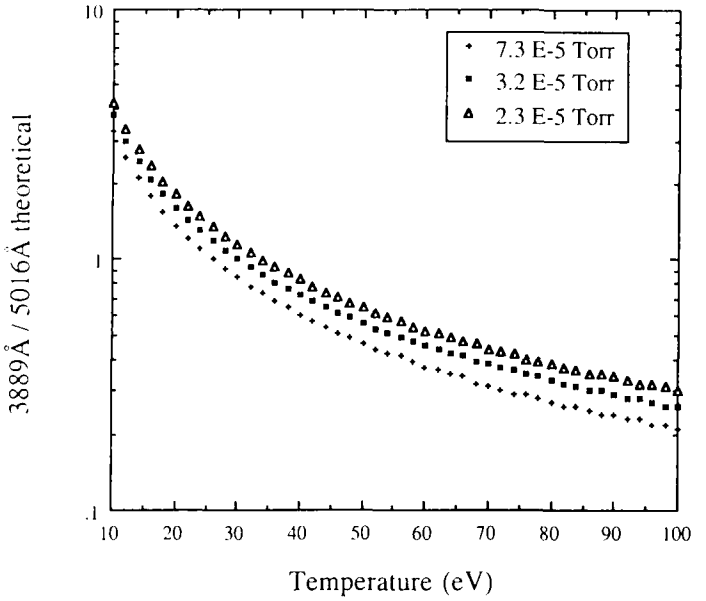

Fig. 4. Theoretical line ratio versus electron temperature for several values of neutral helium pressure.

where n_g is the density of neutral helium in the ground state (1^1S), n_+ is the density of singly ionized helium ions, and the subscripts 4 and 3 denote the upper and lower states of the He II line. The intensity of a neutral helium line (for example, 3889 Å) is simply

$$I_{3889} = \frac{n_{3^3P}}{\tau_{3^3P}} B_{3^3P \to 2^3S} \tag{17}$$

so combining Eqs. (16) and (17), we have

$$\frac{n_+}{n_g} = \frac{1}{K_{+\to 4}} \left[\frac{I_{4686}}{I_{3889}} \frac{n_{3^3P}}{n_e n_g} \frac{B_{3^3P \to 2^3S}}{\tau_{3^3P} B_{4\to 3}} - K_{g\to 4} \right] \tag{18}$$

Since the electron temperature was found by the neutral line ratio measurements, n_{3^3P}/n_g and the rate constants $K_{+\to 4}$ and $K_{g\to 4}$ can be calculated. It is necessary to relate the neutral density outside of the plasma, n_{out}, to that inside the plasma, n_g. This relationship is derived by equating the neutral particle influx to the neutral particle outflux and the rate of burn-up of neutrals by ionization[24]:

$$\frac{n_g}{n_{\text{out}}} = \frac{(1/2) v_0 [S_a/V]}{(1/2) v_0 [S_a/V] + n_e K_{g\to +}} \tag{19}$$

where S_a is the surface area of the plasma, V is the volume of the plasma, and v_0 is the thermal velocity of the neutral helium atom. The plasma is shaped like a bow-tie with one end twisted about the center by 90°. It has a circular cross section at the midplane and an elliptical cross section at each end. The area and volume of the plasma are calculated from the geometry of the magnetic field lines. An ionization gauge provides a measure of n_{out}. For the parameter range under consideration here, the ratio n_g/n_{out} is between 0.92 and 0.98. Thus, with a measure of n_g, we can find n_+ from Eq. (18).

3. LANGMUIR PROBE MEASUREMENTS

Electrostatic probes have been used extensively to measure plasma parameters in many plasma devices. In theory they are simple devices; however, analysis becomes much more complex when the probe is inserted into an anisotropic electron velocity distribution and a moderate magnetic field, such as found in MIMI. Here the probe is used to obtain a second measurement of the electron temperature which is independent of the spectroscopic method. The probe consists of a tungsten wire (0.003″ diameter) shielded with two stainless steel shields and insulated from each other and the plasma with thin-walled ceramic tubing. The stainless steel shields serve both to increase the bandwidth of the probe and to act as an rf shield to shield the tungsten center conductor from plasma noise and oscillations. The probe is inserted radially as shown in Fig. 5. The center conductor extends into the plasma 1 cm from the probe tip and is oriented parallel to the magnetic field. All other parts visible to the plasma are covered with insulating ceramic. The voltage applied to the probe (typically −150 to 150 V) is approximately one cycle of a sine wave with a 50-μs period. The present sweeping circuit (Fig. 6) is a modified design of Friedman.[25] The current and voltage traces are stored simultaneously using a 100-MHz digitizer, and an I-V curve is extracted. A typical I-V characteristic is shown in Fig. 7.

If it is assumed that the electron energy distribution is Maxwellian, then Laframboise[26] has shown the electron current to be equal to

$$I_e = Aen_e \sqrt{\frac{kT_e}{2\pi m_e}} \exp\left(\frac{-e(V_p - V_s)}{kT_e}\right) \tag{20}$$

where A is the surface area of the probe, n_e is the electron density, m_e is the electron mass, V_p is the probe potential, and V_s is the space (or plasma) potential. Dunn and Liordi[27] have shown that Laframboise's theory can be applied to the orbital-motion-limited region of probe operation for $1 \leq r_p/\lambda_d \leq 2$, where r_p is the probe radius and λ_d is the Debye length. It

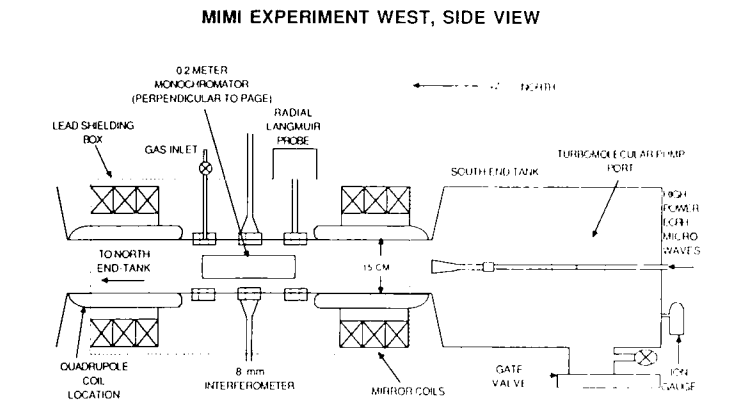

Fig. 5. Experimental configuration: MIMI

is within this range that the Langmuir probe in MIMI operates. From a plot of the natural logarithm of the electron current versus the probe potential, the slope is equal to the inverse of the electron temperature.

4. EXPERIMENTAL CONFIGURATION

Figure 5 shows a schematic diagram of the experiment. MIMI produces a nonaxisymmetric mirror plasma by means of whistler-mode electron-cyclotron-resonance heating. (Further details on MIMI can be found in Refs.1 and 28.) The microwaves have a frequency of 7.43 GHz at a power of 400–900 W. The forward and reflected power were measured by a directional coupler and calibrated diodes. A leak valve in the midplane region provided a way to control the pressure of the gas released into the vacuum vessel. Pressure measurements were made with an ionization gauge located in the north end tank. A 0.2-m scanning monochromator (Acton Research

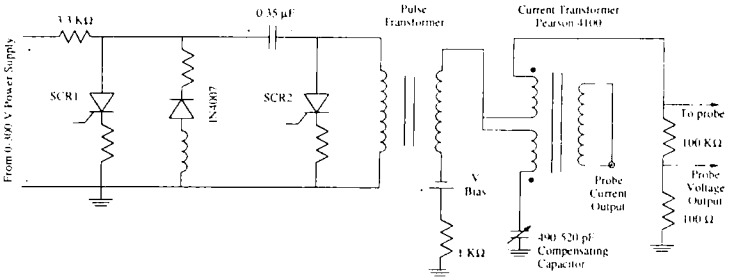

Fig. 6. Langmuir probe sweeping circuit.

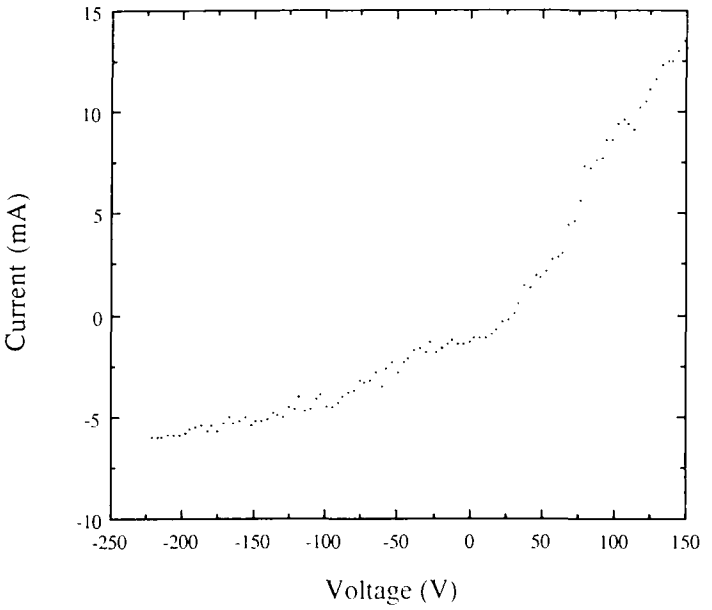

Fig. 7. Sample $I-V$ characteristic of Langmuir probe.

Corp. Model VM-502) was used with a 1200 groove/mm grating, and a side window photomultiplier tube was used as a detector. The plasma was pulsed at the rate of 40 pulses per minute.

The output signal from the photomultiplier was averaged over 10 plasma shots. A background subtraction was done for each line measurement. The data were also corrected for the unequal response of the optical system and detector to different wavelengths using a tungsten filament calibration lamp. Figure 8 shows typical output from the monochromator, microwave interferometer, and forward and reflected power measurements.

5. RESULTS

5.1. Electron Temperature

Figures 9, 10, 12, and 13 show the electron temperature as a function of pressure and microwave power for several line ratios. By averaging 10 plasma shots, the statistical error in the intensity measurement can be made less than 2%. Thus, the major source of error in this analysis is from uncertainties in the cross-section data. Although the shapes of the excitation functions are fairly well known (to ±5%[29]), the absolute peak values are less accurate (10–20%). The line ratios in these figures all show the same

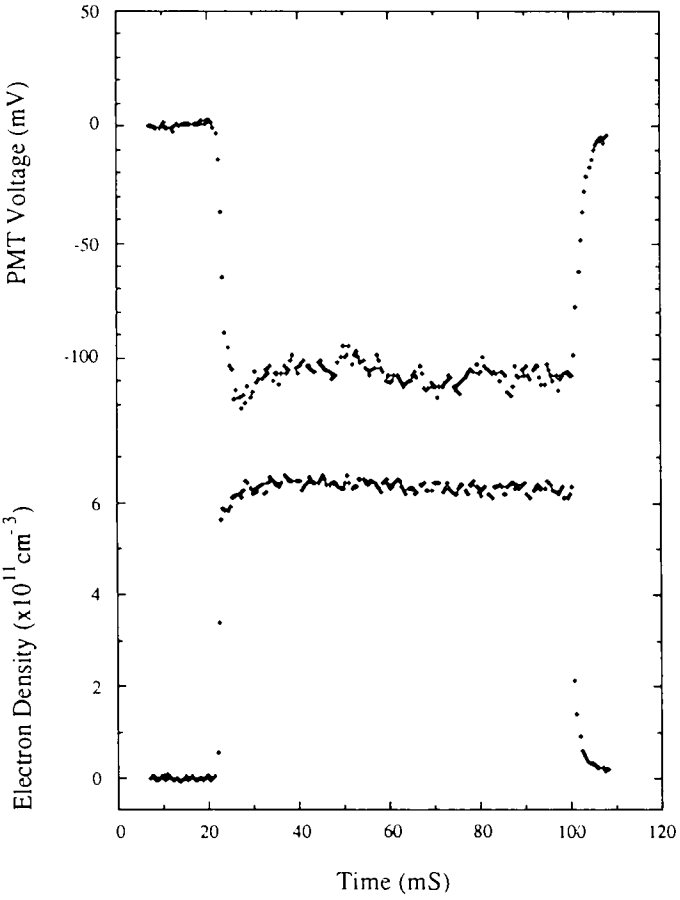

Fig. 8a. Sample signal of photomultiplier tube (top) and microwave interferometer (bottom).

temperature dependence but are offset from each other by this uncertainty in the absolute value of the cross sections involved. The most reliable line ratio utilizes the 3889 and 5016 Å lines. These lines originate from the $n = 3$ level where excitation transfer is less important. However, the 5016 Å line is strongly affected by the imprisonment of radiation. The possibility of other processes occurring in the plasma that have not been taken into account could contribute to error in the measurements.

5.2. Pressure

Figures 9 and 10 show the dependence of the electron temperature on the pressure of the helium gas at the midplane. As these figures show, the

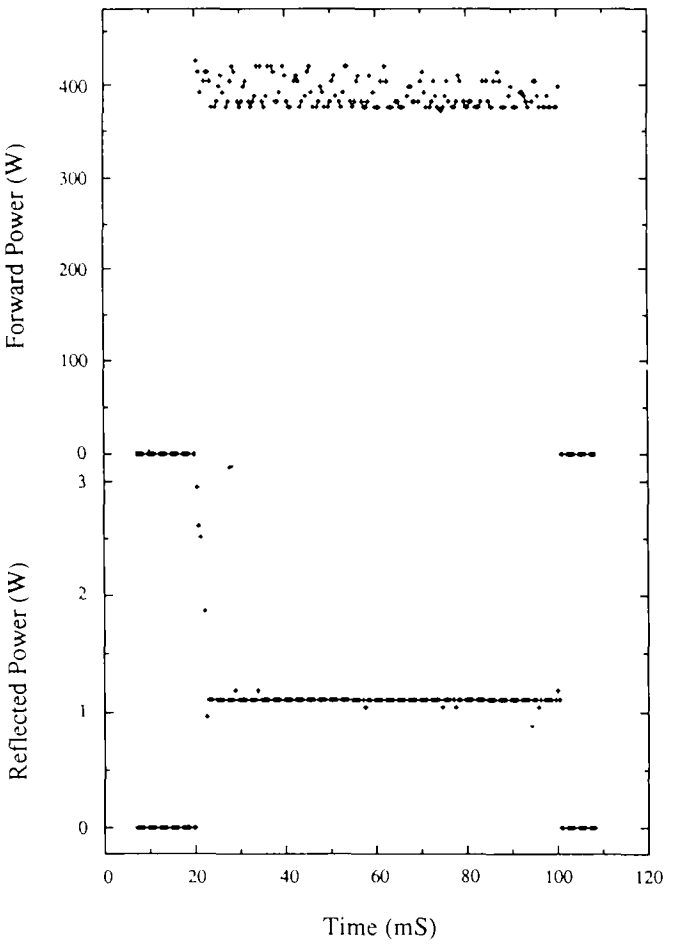

Fig. 8b. Sample signal of forward (top) and reflected (bottom) microwave power. The forward power averages 400 W and the reflected power averages 1 W after an initial spike of 3 W during plasma formation.

electron temperature decreases with increasing pressure. This can be understood by examining the major processes which affect the electrons. The electron distribution in MIMI consists of two electron populations, "hot" and "cold." The hot electrons have been found to have a temperature in the 1–10 keV range[30] and are created by the ECR heating. Because of their large energy, they do not contribute directly to the excitation of neutral helium atoms. The secondary electrons that the hot electrons produce through ionization of the helium are what we call the cold electrons. It is

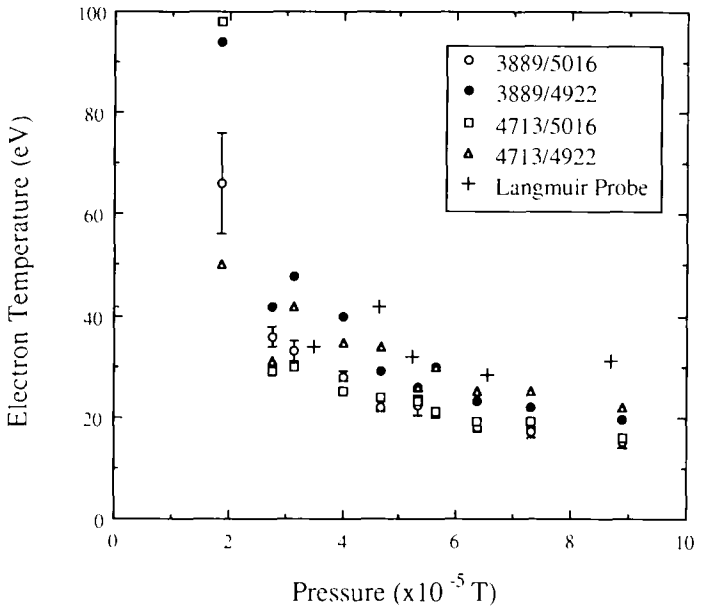

Fig. 9. Electron temperature versus helium pressure for a forward power of 675 W. Error bars are shown for the 3889/5016 line ratio; the error bars for the other line ratios are similar and have been omitted for clarity.

these cold electrons that produce the majority of the helium excitation. In the steady state a balance is reached between the "ionization-cooling" and ECR heating so that both a hot and cold population will exist simultaneously. The particle balance equations for the cold electrons, the hot electrons, and the ions are

$$\frac{d}{dt} n_c = n_c n_g \langle \sigma v \rangle^c_{1\to 11} + n_c n_+ \langle \sigma v \rangle^c_{11\to 111} + n_h n_g \langle \sigma v \rangle^h_{1\to 11} \tag{21}$$

$$+ n_h n_+ \langle \sigma v \rangle^h_{11\to 111} - \frac{n_c}{\tau_c} - \frac{n_c}{\tau_{c\to h}}$$

$$\frac{d}{dt} n_h = \frac{n_c}{\tau_{c\to h}} - \frac{n_h}{\tau_h} \tag{22}$$

$$\frac{d}{dt} n_+ = n_c n_g \langle \sigma v \rangle^c_{1\to 11} + n_h n_g \langle \sigma v \rangle^h_{1\to 11} - n_c n_+ \langle \sigma v \rangle^c_{11\to 111} \tag{23}$$

$$- n_c n_+ \langle \sigma v \rangle^c_{11\to 111} - n_h n_+ \langle \sigma v \rangle^h_{11\to 111} - \frac{n_+}{\tau_+}$$

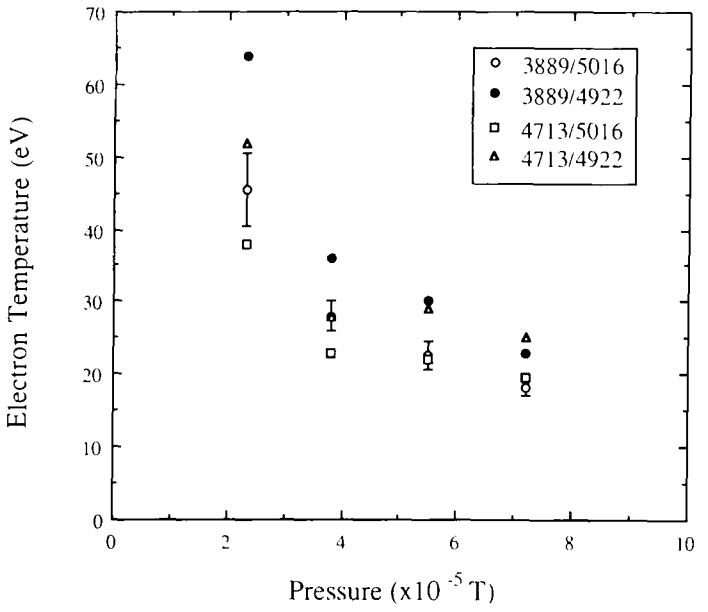

Fig. 10. Electron temperature versus helium pressure for a forward power of 750 W.

Here $\tau_{c\to h}$ is the time it takes for a cold electron to be heated by ECRH into the hot electron population, and c, h, and + denote cold, hot, and ion, respectively. The confinement time for the cold electrons, τ_c, should be approximately equal to the ion confinement time τ_+ since ambipolar diffusion governs their loss from the mirror. The smaller hot electron population is magnetically confined and has $\tau_h \gg \tau_c$. Assuming steady state, we can combine these equations to produce

$$\frac{1}{n_g \tau_c} \approx \langle \sigma v \rangle^c_{1\to 11} \left\{ 1 + \frac{n_h}{n_c} \frac{\langle \sigma v \rangle^h_{1\to 11}}{\langle \sigma v \rangle^c_{1\to 11}} \right\} \tag{24}$$

Since the second term in the brackets of Eq. (24) is small compared to 1, we see that $\langle \sigma v \rangle$, which is a function of the cold electron temperature, should scale as reciprocal of pressure since τ_c is independent of pressure. Figure 11 shows a plot of the right-hand side of Eq. (24) versus n_g^{-1} using the cold electron temperatures (measured by the 3889 Å/5016 Å line ratio) for the data of Fig. 9. In the temperature range for this plasma the ionization rate $\langle \sigma v \rangle$ is an increasing function of electron temperature and therefore Fig. 11 implies that the temperature increases with n_g^{-1}. Measurements on other ECR mirror plasmas[31] (H_2 and N_2) have shown a similar decrease in temperature as the pressure increases.

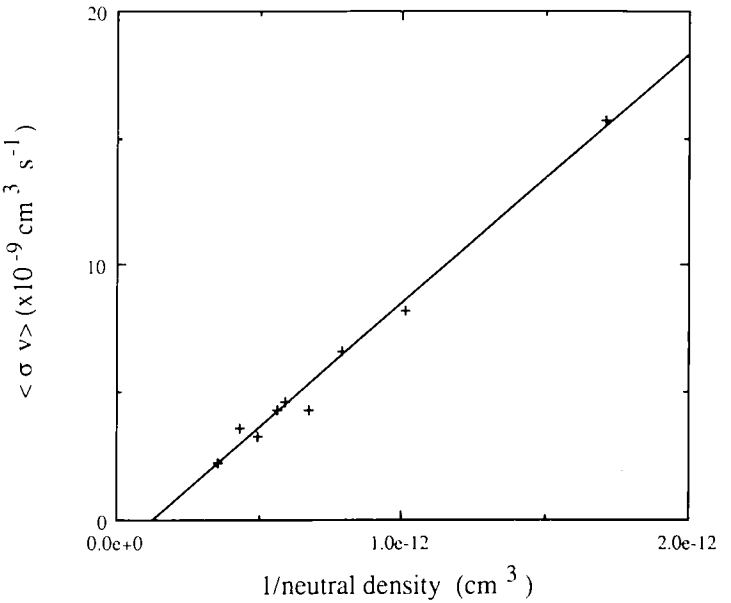

Fig. 11. Helium ionization rate $\langle \sigma v \rangle$ versus reciprocal of neutral helium density within the plasma.

The line of Fig. 11 represents a least-squares fit to the data, and from the slope of this line the confinement time τ_c is measured to be 0.10 ms. The confinement time can also be calculated from the Pastukhov and flow-confinement model[32] to be $(0.085 + 0.306/n_+)$ ms, with n_+ in units of 10^{11} cm^{-3}. For a typical ion density of 4×10^{11} cm^{-3} (see Figs. 15–18) this predicts a confinement time on the order of 0.16 ms. The theoretical confinement time depends upon several poorly known parameters, such as the ion temperature, plasma length, and the ambipolar potential. Therefore a discrepancy of 60% between theory and measurement is not unreasonable.

5.3. Microwave Power

Figures 12 and 13 show a slight dependence of the electron temperature on the forward power. The Langmuir probe data of Fig. 13 were taken at a slightly different operating pressure and are thus offset from the electron temperatures determined from the optical spectroscopy; however, they do show a similar dependence on the microwave power.

Previous measurements with diamagnetic loops[30] have shown that the amount of microwave power absorbed per unit volume of plasma increases as the forward power is increased. Other work[33] has shown that the

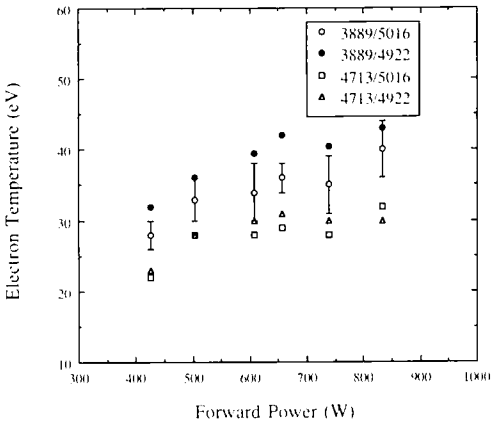

Fig. 12. Electron temperature versus forward microwave power for a pressure of $P = 2.8 \times 10^{-5}$ Torr.

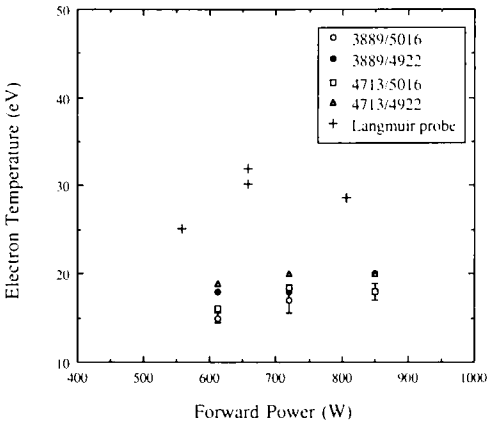

Fig. 13. Electron temperature versus forward microwave power for $P = 7.0 \times 10^{-5}$ Torr. Note that Langmuir probe measurements are taken at a lower pressure ($P = 4.6 \times 10^{-5}$ Torr) which makes the temperature higher, as indicated by Figs. 9 and 10.

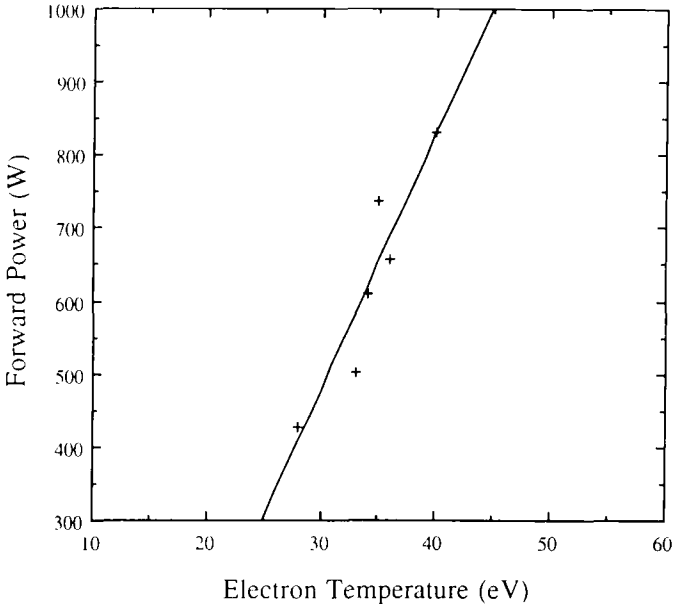

Fig. 14. Forward microwave power versus electron temperature.

microwaves are strongly coupled to the hot electrons with an absorption efficiency on the order of 0.90. Thus, as the microwave power is increased, the primary effect on the plasma is to increase the density and temperature of the hot electrons.[34] Green[35] has calculated the energy differential ionization cross section for a number of atomic species, including helium. Using this cross section and a Maxwellian distribution of primary electrons having a temperature of 4 keV, we find the temperature of the secondary electron distribution to be 19 eV. The secondary electron temperature is actually very insensitive to the temperature of the primary electrons for the range of interest (1–10 keV). Therefore any increase that we measure in the cold electron temperature is due to the weak coupling of the microwaves to the cold bulk plasma. The power balance equation for the cold electrons is

$$\frac{n_c}{\tau_c} kT_c + e\Phi_i \langle \sigma v \rangle_{I \to II}^{c} n_g n_c = \frac{\eta P}{V} \tag{25}$$

where c denotes cold, Φ_i is the ionization potential of helium, η is the absorption efficiency of the cold electrons, P_{ECH} is the ECH microwave power, and V is the volume of the plasma. Substituting in the result of

Eq. (24) yields

$$P = \frac{n_e}{\tau_e} \frac{V}{\eta} (kT_e + e\Phi_i) \tag{26}$$

Figure 14 shows the data of Figure 12 plotted as power versus temperature with the line representing a least-squares fit to the data. When typical values of $n_e = 6 \times 10^{11}$ cm^{-3} (from microwave interferometer measurements), $\tau_e =$ 0.1 ms (from Fig. 11), $V = 2500$ cm^3, and $\eta = 0.10$ are used, Eq. (27) gives an order-of-magnitude estimate of the slope of Fig. 14 to be 24 s^{-1} while the measured slope is 35 s^{-1}. The measured electron temperature variation with microwave power is therefore consistent with weak absorption of microwaves by the cold electrons.

5.4. Ion Density

Figures 15–18 display the ion density (from ion-to-neutral line intensity ratio measurements) and total electron density (from microwave interferometer measurements) as a function of forward power and pressure. These plots seem to show little variation with either the pressure or the power. The ion density calculation is more uncertain than the previous temperature measurements due to the lack of data on electron impact excitation of ions. The ion and electron density would be expected to be equal; however, contributions from impurity ions and from fully stripped helium cause the electron density to be slightly greater than the ion density.

6. CONCLUSIONS

In this experiment we have determined the electron temperature of helium plasmas and its dependence upon the operating parameters of the Michigan mirror machine. A model has been developed which takes into account the important collisional and radiative processes occurring in the plasma. This model examines secondary processes such as imprisonment of resonance radiation, excitation transfer between levels, and excitation from metastable states. The model could also be used to diagnose other plasmas having a similar electron density and electron temperature. If the electron temperature is less than 10 eV, the tail of the electron distribution will do the majority of the excitation, and any deviations from a Maxwellian distribution will become important. If the electron distribution function is known, it could be used instead of a Maxwellian in Eq. (7). In the present experiment, the cold electrons dominate these processes and the hot electron tail can be neglected.

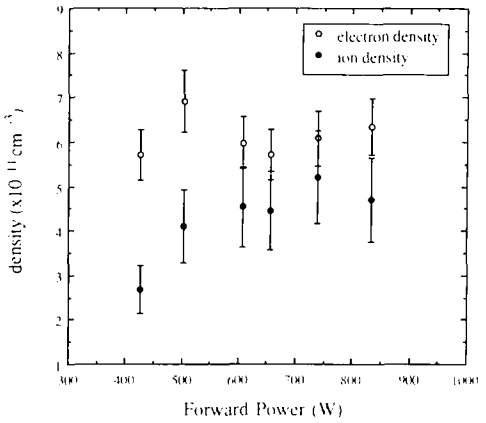

Fig. 15. Electron density (from microwave interferometer measurement) and ion density (from ion-to-neutral line intensity ratio measurement) versus forward microwave power for a pressure of $P = 2.8 \times 10^{-5}$ Torr.

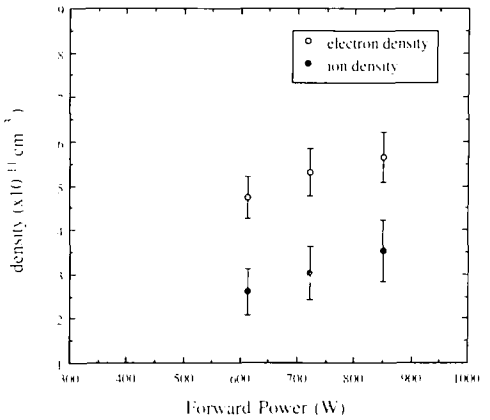

Fig. 16. Electron and ion density versus forward microwave power for a pressure of $P = 7.0 \times 10^{-5}$ Torr.

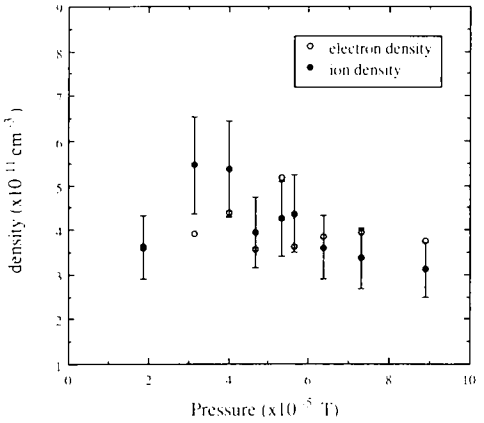

Fig. 17. Electron and ion density versus pressure for a forward microwave power of 675 W. Error bars for the electron density are similar to those of Figs. 15 and 16 and have been omitted for clarity.

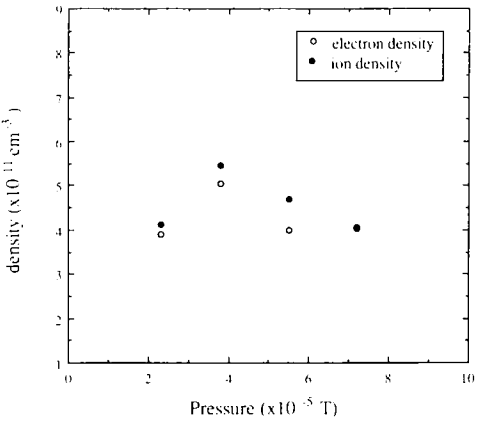

Fig. 18. Electron and ion density versus pressure for a forward microwave power of 750 W. Error bars are similar to those of Figs. 15 and 16 and have been omitted for clarity.

By far the most important parameter is the pressure of the helium fill gas. It was found that the electron temperature ranges from 60 to 20 eV over the operating regime of MIMI (1×10^{-5} to 1×10^{-4} Torr), while the electron density stays approximately constant at $2\text{–}5.5\times10^{11}\,\text{cm}^{-3}$. The electron temperatures measured from the ratios of neutral lines match Langmuir probe data fairly well and ion density measurements from an ion-to-neutral line ratio match the electron density measurements of a microwave interferometer very well.

7. APPENDIX

7.1. Choice of Cross-Section Data

The use of this method to determine electron temperatures depends upon the accurate knowledge of electron impact excitation cross sections between various states of neutral helium. A recent review of electron impact optical excitation functions by Heddle and Gallagher[36] provides an excellent survey of cross-section measurements from the ground state. Theoretical calculations by Mewe[37] provide excitation cross sections for ions. Ionizations rates for neutral and singly ionized helium have been compiled by Bell.[38]

7.2. Excitations from Metastable States 2^1S and 2^3S

Flannery *et al.*[39] have calculated cross sections from 2^1S to 2^1P, 3^1S, 3^1P, 3^1D, and 4^1P for electron energies from threshold to 400 eV. Measurements by Rall *et al.*[40] were used for excitation from the 2^3S metastable state.

7.3. Ionization of 2^1S and 2^3S

Cross section values have been measured by Dixon *et al.*[41] and these agree well with the theoretical studies of Ton-That *et al.*[42]

7.4. Excitation Transfers

The accuracy of Eq. (16) has been tested against calculations done for the $2^3S \rightarrow 2^3P$ transition by Flannery *et al.*[43] and are found to agree within 20% when the electron energy is more than a few times the threshold energy.

7.5. Lifetimes and Transition Probabilities

A thorough compilation of transition probabilities has been done by Theodosiou,[44] which agrees well with the values of Wiese.[45]

ACKNOWLEDGMENTS

This project was supported by the National Science Foundation. One of us (K.L.J.) would like to thank the U.S. Department of Energy for providing a Magnetic Fusion Technology Fellowship.

REFERENCES

1. J. Booske, W. Getty, R. Gilgenbach, and R. Jong, *Phys. Fluids* **28**, 3116 (1985).
2. O. Popov, *J. Vac. Sci. Technol. A* **7**, 914 (1989).
3. K. Suzuki, K. Ninomiya, S. Hishimatsu, and S. Okudaira, *J. Vac. Sci. Technol. B* **3**, 1925 (1985).
4. N. Sakudo, T. Tokiguchi, H. Koike and I. Kanomata, *Rev. Sci. Instrum.* **54**, 681 (1983).
5. S. Matsuo and Y. Adachi, *Jpn. J. Appl. Phys.* **21**, L4 (1982).
6. M. Matsuoka and K. Ono, *J. Vac. Sci. Technol. A* **6**, 25 (1988).
7. J. Forster and W. Holber, *J. Vav. Sci. Technol. A* **7**, 899 (1989).
8. J. McKillop, J. Forster, and W. Holber, *Appl. Phys. Lett.* **55**, 30 (1989).
9. S. Cunningham, Conference on Thermonuclear Reactions, University of California Radiation Lab, Livermore, U.S. Atomic Energy Commision, Rep. No. 279, 289 (1955).
10. R. Sovie, *Phys. Fluids* **7**, 613 (1964).
11. B. Eastlund *et al.*, *J. Appl. Phys.* **44**, 4930 (1973).
12. H. Drawin, *Z. Naturforsch.* **19a**, 1451 (1964).
13. H. Drawin, *Z. Naturforsch.* **22a**, 587 (1967).
14. R. DeVries, and R. Mewe, *Phys. Fluids* **9**, 414 (1966).
15. R. Mewe, *Br. J. Appl. Phys.* **17**, 1239 (1967).
16. N. Brenning, *J. Quant. Spectrosc. Radiat. Transfer* **24**, 293 (1980).
17. N. Brenning, *J. Phys. D* **13**, 1459 (1980).
18. H. Drawin, F. Emard, K. Katsonis, *Z. Naturforsch.* **28a**, 1422 (1973).
19. A. Phelps, *Phys. Rev.* **110**, 1362 (1958).
20. E. Kingston, *J. Phys. B.* **1**, 559 (1968).
21. H. Drawin, EUR-CEA-FC-383, Euratom Report (1966).
22. H. Bethe and E. Salpeter, *Handbuch Phys.* **35**, 349 (1957).
23. G. Arfken, *Mathematical Methods for Physicists*, Academic Press, New York (1985), p. 182.
24. H. West, Lawrence Livermore National Laboratory Report No. UCRL-53391 (1982).
25. W. Friedman, *Rev. Sci. Instrum.* **42**, 963 (1971).
26. J. G. Laframboise, "Theory of Spherical and Cylindrical Langmuir Probes in a Collisionless, Maxwellian Plasma at Rest," UTIAS Report No. 100 (1966).
27. M. G. Dunn and J. A. Liordi, *AIAA J.* **8**, 1077 (1970).
28. T. Goodman, "Characterization of an Electron-Cyclotron-Resonance-Heated Mirror Plasma as a Soft X-Ray Source for X-Ray Lithography," PhD Thesis, University of Michigan (1989).
29. R. St John *et al.*, *Phys. Rev.* **134**, A888 (1964).
30. J. Booske, "Whistler-Mode Electron-Cyclotron-Resonance Heating and Emission in a Magnetic Mirror Plasma," PhD Thesis, University of Michigan (1985), p. 40.
31. H. Amemiya, K. Shimizu, S. Kato, and Y. Sakamoto, *Jpn. J. Appl. Phys.* **27**, L927 (1988).
32. T. Rognlien and T. Cutler, *Nucl. Fusion* **20**, 1003 (1980).
33. C. C. Petty, "Confinement of multiply charged ions in an ECRH mirror plasma," PhD Thesis, Massachusetts Institute of Technology (1989).
34. Y. Arata, S. Miyake, and H. Kishimoto, *Jpn. J. Appl. Phys.* **26**, 2072 (1987).

35. A. E. S. Green and T. Sawada, *J. Atmos. Terr. Phys.* **34**, 1719 (1972).
36. D. Heddle and J. Gallagher, *Rev. Mod. Phys.* **61**, 221 (1989).
37. R. Mewe, *Astron. Astrophys.* **20**, 215 (1972).
38. J. Bell, *J. Phys. Chem. Ref. Data* **12**, 896 (1983).
39. M. Flannery *et al.*, *J. Appl. Phys.* **46**, 1186 (1975).
40. D. Rall *et al.*, *Phys. Rev. Lett.* **62**, 2253 (1989).
41. A. Dixon *et al.*, *J. Phys. B* **9**, 2617 (1976).
42. D. Ton-That *et al.*, *J. Phys. B* **10**, 621 (1977).
43. M. Flannery *et al.*, *J. Appl. Phys.* **46**, 1186 (1975).
44. C. Theodosiou, *At. Data Nucl. Data Tables* **36**, 98 (1987).
45. W. Wiese *et al.*, *Atomic Transition Probabilities*, National Bureau of Standards Publication No. NSRDS-NBS4 (1966).